Future Projection of Ocean Wave Climate: Analysis of SST Impacts on Wave Climate Changes in the Western North Pacific

TOMOYA SHIMURA

Graduate School of Engineering, Kyoto University, Kyoto, Japan

NOBUHITO MORI AND HAJIME MASE

Disaster Prevention Research Institute, Kyoto University, Kyoto, Japan

ABSTRACT

Changes in ocean surface waves elicit a variety of impacts on coastal environments. To assess the future changes in the ocean surface wave climate, several future projections of global wave climate have been simulated in previous studies. However, previously there has been little discussion about the causes behind changes in the future wave climate and the differences between projections. The objective of this study is to estimate the future changes in mean wave climate and the sensitivity of the wave climate to sea surface temperature (SST) conditions in an effort to understand the mechanism behind the wave climate changes by specifically looking at spatial SST variation. A series of wave climate projections forced by surface winds from the MRI-AGCM3.2 were conducted based on SST ensemble experiments. The results yield future changes in annual mean wave height that are within about ±0.3 m. The future changes in summertime wave height in the western North Pacific (WNP), which are influenced by tropical cyclone changes, are highly sensitive to SST conditions. To generalize the result, the wave climate change and SST relation found by this study was compared with multimodel wave ensemble products from the Coordinated Ocean Wave Climate Project (COWCLIP). The spatial variation of SST in the tropical Pacific Ocean is a major factor in the wave climate changes for the WNP during summer.

1. Introduction

The number of studies assessing the impact of long-term change in oceanographic phenomena (especially the impact of sea level rise) related to climate change has been increasing (e.g., Hallegatte et al. 2013). Changes in ocean surface gravity waves (denoted as waves hereinafter) produce impacts for a variety of disciplines. Ocean waves are one of the key components of beach morphology (Short 1999), and wave energy may be a promising renewable energy source (Cruz 2008). Changes in long-term wave climate have been observed by voluntary observing ships (Gulev and Grigorieva 2004), reanalysis data (e.g., Wang and Swail 2001; Semedo et al. 2011), satellite imagery (Hemer et al. 2010; Young et al. 2011), and buoy data (e.g., Menéndez et al. 2008).

Impacts of long-term wave climate variability and change have also been reported. Kuriyama et al. (2012) found that, for a span of 22 years, the interannual shoreline variation at the Japanese coast has been induced by the fluctuation of the deep-water wave energy flux. Sasaki (2012) estimated climatological annual mean wave energy around Japan based on 30 years of observations and found an increasing trend caused by more frequent swells. Furthermore, wave inundation has occurred across the western tropical Pacific, and recent accelerated sea level rise has contributed to the severity of the impact (Hoeke et al. 2013).

A few studies have assessed impacts of future changes in wave climate using future wave climate projections under greenhouse gas emission scenarios. For example, Suh et al. (2012) examined the impact of climate change on a caisson-type breakwater, including the effect of changes in wave height at the end of this century. Charles et al. (2012) projected future wave climate for the Bay of Biscay and concluded that changes in wave conditions are leading to a decrease in the annual

Corresponding author address: Tomoya Shimura, Graduate School of Engineering, Kyoto University, Katsura, Kyoto 615-8530, Japan.
E-mail: shimura.tomoya.36w@st.kyoto-u.ac.jp

net longshore drift. The quantitative projection of future wave climate, including the likely expected range of the future change, is information that would be very useful to assess coastal impacts and how coastal communities will need to adapt. Using a global climate model for climate projections helps provide an overview of the system and the nature of the contributing factors. This, in turn, helps yield information about future impacts and allows for strategic planning to address these impacts in a more rational way.

To assess the future changes in wave climate, several future projections of global wave climate have been conducted using different forcing mechanisms and wave models (Mori et al. 2010, hereinafter MO10; Dobrynin et al. 2012; Hemer et al. 2013b, hereinafter HE13; Fan et al. 2013, hereinafter FA13; Semedo et al. 2013, hereinafter SE13) and statistical models (Wang and Swail 2006; Mori et al. 2013). Consequently, multimodel ensemble projections of global wave climate have been carried out in the Coordinated Ocean Wave Climate Project (COWCLIP; Hemer et al. 2012, 2013a; Stocker et al. 2013). The results of five independent studies (Wang and Swail 2006; MO10; HE13; FA13; SE13) showed consistent future changes in mean wave climate among models: future increases in wave height over the Southern Ocean and decreases in wave height in the subtropics (Hemer et al. 2013a). However, there is little discussion about the cause of changes in future wave climate and the differences between model projections. Confidence in the projections is greatest if we understand the relationship between external forcing and the physical processes (Knutti et al. 2013).

A dynamical approach of global wave projection has been developed over the last few years (MO10; HE13; FA13; SE13), and this approach is employed by this study. A framework of the approach can be described as follows:

1) A global climate simulation by an atmosphere–ocean coupled global climate model under an emission scenario.
2) A global atmospheric climate simulation by an atmospheric GCM using sea surface temperature data from the AOGCM as a boundary condition.
3) A global wave simulation by a wave model forced with the sea surface winds of the AGCM.

The procedure in item 2 is sometimes skipped (Dobrynin et al. 2012), but the climate projection with an AGCM is useful for impact assessments because the AGCM has a finer spatial resolution over an AOGCM, with lengths in the range of 20–100 km, generally.

The choice of SST is arbitrary for the AGCM; an ensemble-mean SST of several AOGCMs is sometimes used for a simulation. SST, however, can lead to a fundamental variation in the general circulation and yield significant impacts on the wave climate projection through the sea surface wind. Therefore, it is important to estimate the sensitivity of a wave climate projection to projected SST. It is difficult to understand the mechanisms of future wave change with an arbitrary choice of GCM because there are many different factors behind future projections beside SST, such as cloud physics, advection scheme, radiation scheme, and grid resolution, etc. The analysis of SST ensemble experiments is useful to understand the role of SST while neglecting other factors (numerical scheme, etc.).

The objective of this study is to estimate the response and the sensitivity of mean wave climate to projected SST and to understand the mechanism behind climate forcing by specifically looking at spatial SST variation in the future climate. A series of wave climate projections using the same AGCM is conducted based on SST ensemble experiments. First, this study shows the response and the sensitivity of mean significant wave height to projected SST conditions, indicating that future summer wave height in the western North Pacific is sensitive to SST conditions. Second, climatological causes behind future wave climate changes in the WNP are discussed in detail with future SST warming and typhoons. To generalize the results, we consider the perturbed physics ensemble experiments and the multimodel ensemble study (COWCLIP) in addition to SST ensemble experiments.

Wave direction and wave period, as well as significant wave height, are important for coastal process, and they are expected to change significantly in the future (e.g., Hemer et al. 2013a). We, however, mainly deal with significant wave height in this study in order not to complicate discussion, although the future changes in wave period are added in section 5a. Other wave properties will be discussed in a future article.

Abbreviations and acronyms that appear in this paper are listed in the appendix.

2. Methodology

The framework of wave climate projection of this study is the same as that described in the introduction. The methodology of atmospheric climate projection by AGCM using SST projected by AOGCM as the boundary condition is described in section 2a. The methodology of wave climate projection by a wave model forced by the sea surface wind of AGCM is described in section 2b.

a. Atmospheric climate projection

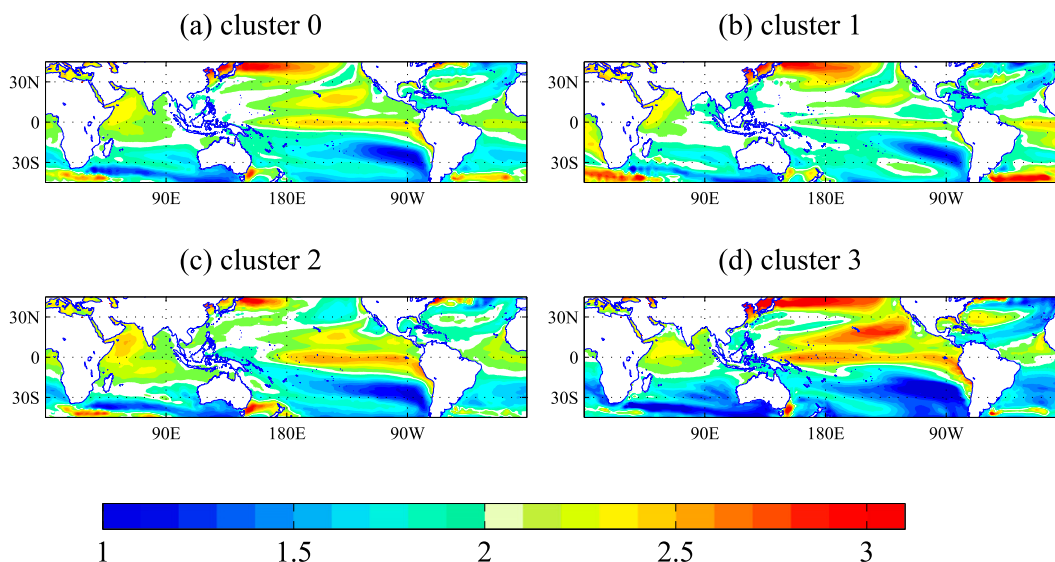The AGCM used in this study, MRI-AGCM3.2 (Mizuta et al. 2012), was developed by the Japanese

FIG. 1. Future changes in annual mean SST for the case of (a) cluster 0, (b) cluster 1, (c) cluster 2, and (d) cluster 3 (°C).

Meteorological Research Institute for IPCC AR5 (Stocker et al. 2013). The SST and perturbed physics ensemble experiments were carried out with the 60-km horizontal spatial resolution model of the MRI-AGCM3.2 (MRI-AGCM3.2H). The forcings used with the AGCM are SST, sea ice at the bottom boundary, and greenhouse gases in the atmosphere.

The time slice experiments were conducted using 1979–2009 for the present climate and 2075–99 for the future climate. Lower boundary conditions of MRI-AGCM3.2H in the present climate were the monthly-mean observed sea ice concentration and SST from the Hadley Centre Sea Ice and Sea Surface Temperature dataset, version 1 (HadISST1; Rayner et al. 2003). The boundary conditions for the future climate consisted of four different statistically analyzed SSTs (Murakami et al. 2012). The four future SST conditions as boundary conditions of MRI-AGCM3.2H were defined based on SSTs projected by 18 models from phase 3 of the Coupled Model Intercomparison Project (Meehl et al. 2007). The first SST condition (denoted as cluster 0) is the ensemble-mean SST projected by 18 models of CMIP3 under the A1B scenario of the Special Report on Emission Scenarios. The other three SST conditions (denoted as clusters 1–3) are differently classified future SST patterns derived by cluster analysis of the future change pattern of SST from 18 CMIP3 models under the A1B emission scenario. The four SSTs can objectively express the representative SSTs of the 18 CMIP3 models because of the cluster analysis. The detail of the clustering analysis of future SST conditions was described in Murakami et al. (2012). Interannual variations of the future climate SST

are given by detrended interannual variations of present climate SST (1979–2003), based on the assumption that the interannual variations of SST in the future climate are similar to those of the present climate.

Figure 1 shows future changes in SST for clusters 0–3. All the SST patterns show that SST in the future climate increases over most of the entire ocean, with increases up to about 3°C. The North Pacific, especially, shows

TABLE 1. The 18 CMIP3 models used for cluster analysis and the SST cluster number (Murakami et al. 2012). (For model names not previously expanded in the appendix, see www.ametsoc.org/PubsAcronymList.)

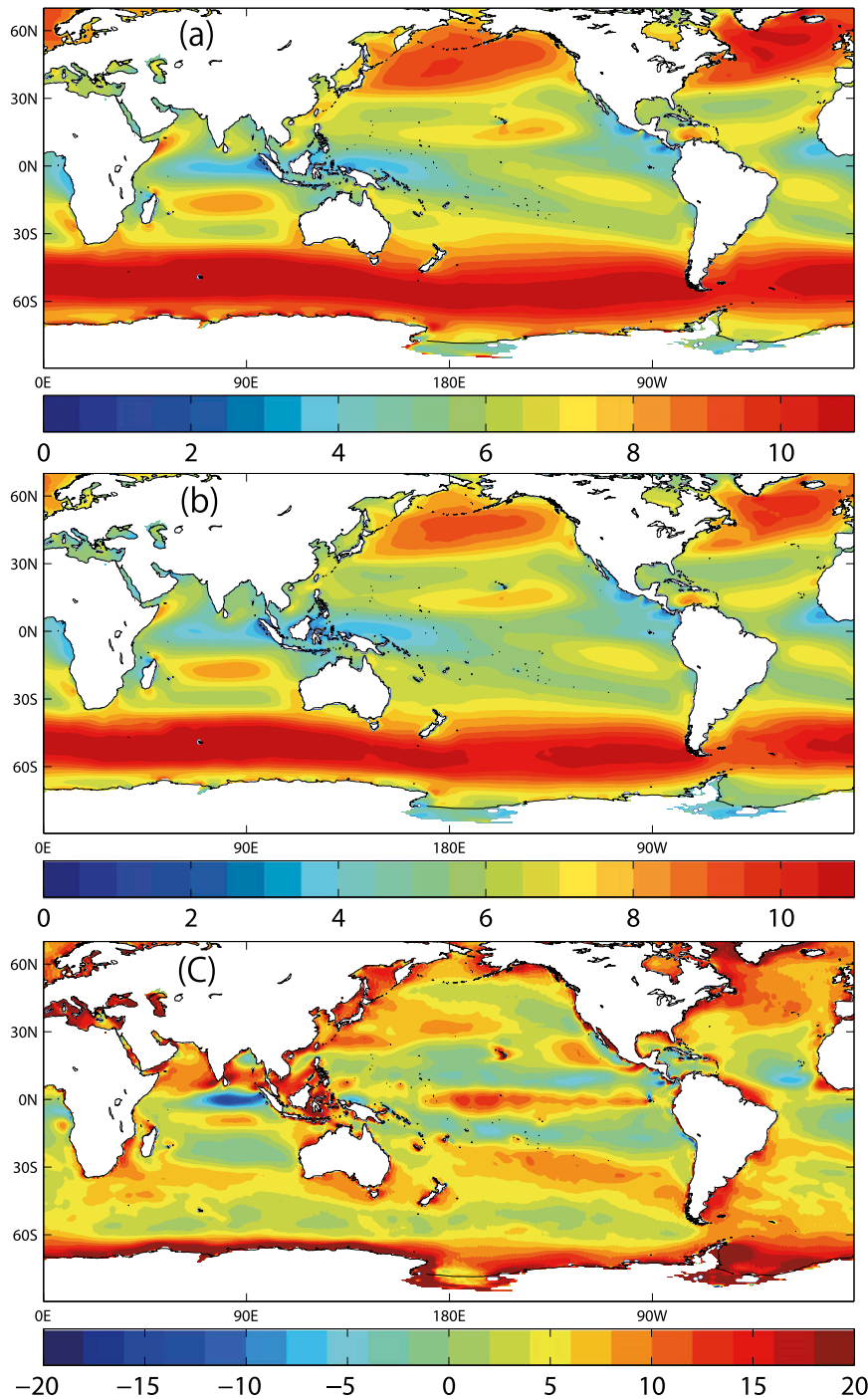| Model name	SST cluster No.	Letters corresponding to models in Fig. 14
BCCR-BCM2.0	1	A
CGCM3.1 T47	2	B
CGCM3.1 T63	2	C
CNRM-CM3	1	D
CSIRO Mk3.0	3	E
GFDL CM2.0	3	F
GFDL CM2.1	3	G
GISS-AOM	1	H
INM-CM3.0	1	I
IPSL-CM4	1	J
MIROC3.2 (hires)	2	K
MIROC3.2 (medres)	2	L
MIUBECHOG	1	M
MPI ECHAM5	2	N
MRI-CGCM2.3	2	O
CCSM3	1	P
HadCM3	3	Q
HadGEMl	3	R

FIG. 2. The $\overline{U_{10}}$ over the period 1979–2009 for (a) HPA (m s^{-1}) and (b) ERA-Interim (m s^{-1}); (c) the difference of HPA and ERA-Interim (normalized by ERA-Interim value; %).

a greater increase in temperature than any other region. The different clusters of SST show different spatial characteristics. Cluster 3 shows the warmest SST, and cluster 1 shows the lowest SST in the tropical Pacific. Cluster 2 shows the warmest SST in the tropical Indian Ocean. The spatial standard deviations of temperature rise in the tropics (30°S–30°N) are 0.24°, 0.21°, 0.27°, and 0.38°C for clusters 0–3, respectively. The SST cluster numbers for 18 CMIP3 models are described in Table 1.
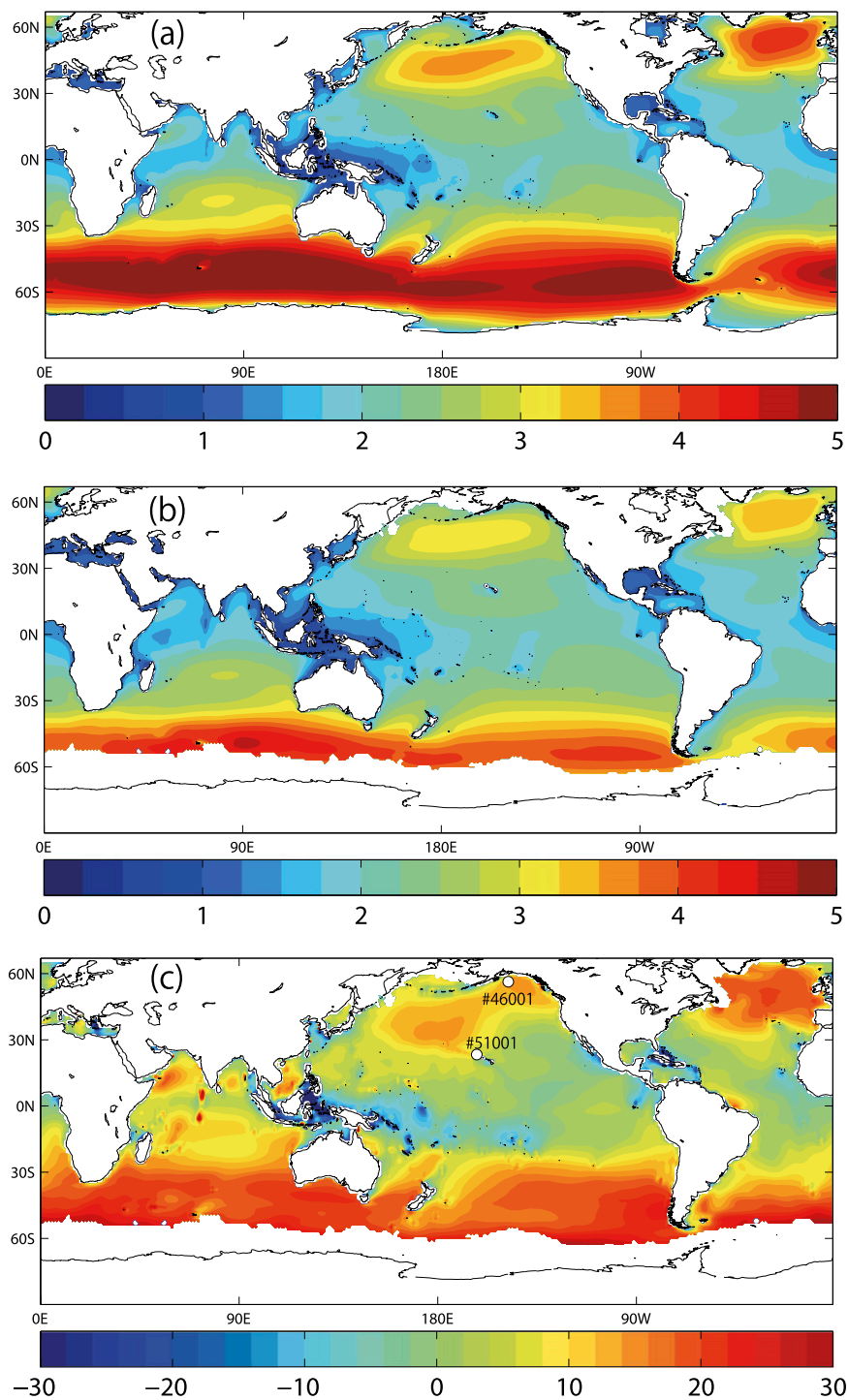
FIG. 3. The $\overline{H_s}$ over the period 1979–2009 for (a) HPA (m) and (b) ERA-Interim (m); (c) the difference of HPA and ERA-Interim (normalized by ERA-Interim value; %). [The white circles labeled with numbers 46001 and 51001 in (c) are buoy locations used in Fig. 4.]
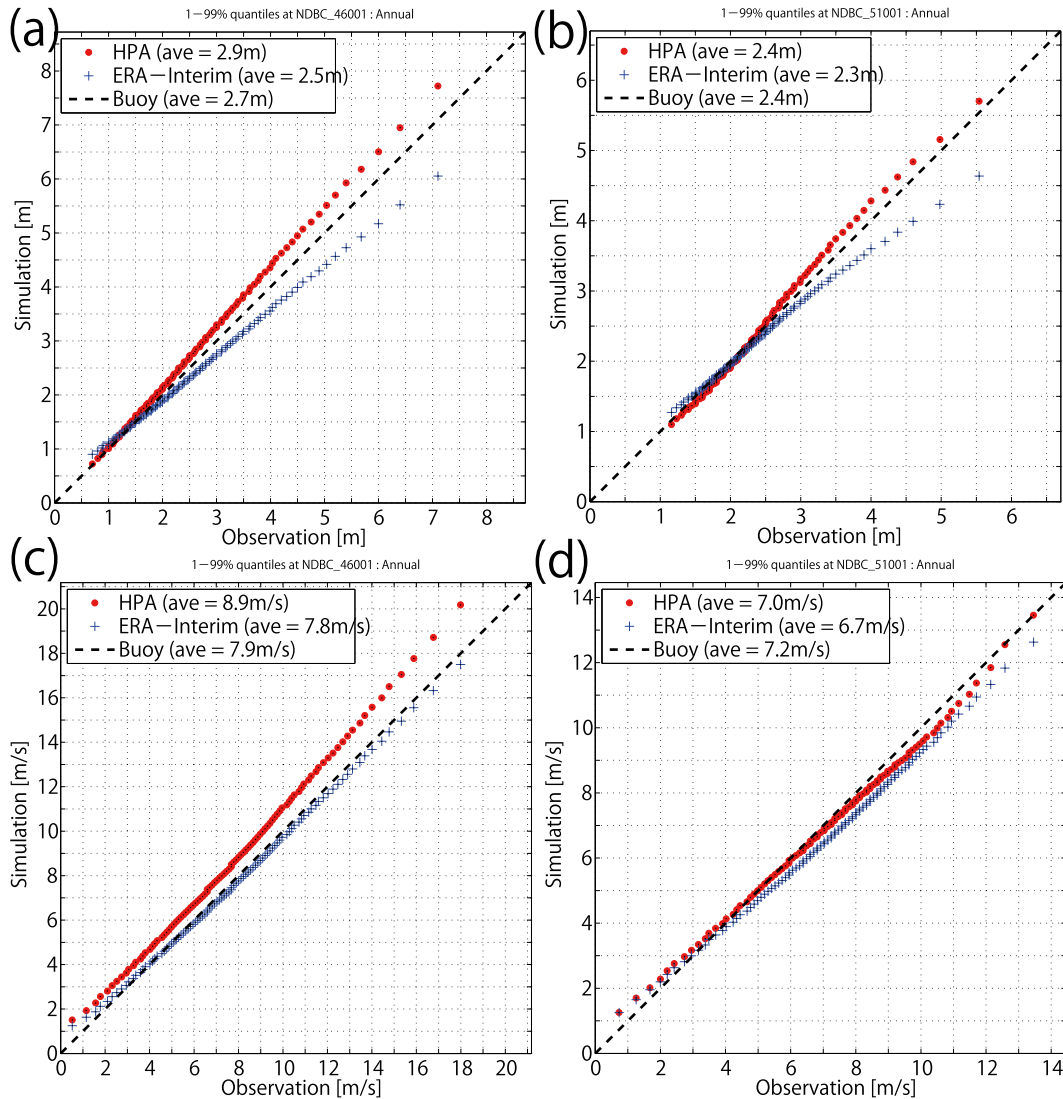
FIG. 4. Quantile–quantile plot (1%, 2%, ..., 99%) for H_s derived from HPA (red dot), ERA-Interim (blue cross), and buoy data (dashed line) from (a) 46001 (56.3°N, 147.9°W) and (b) 51001 (23.4°N, 162.3°W), and for U_{10} from (c) 46001 and (d) 51001. The locations of comparison sites are plotted in Fig. 3c by white circles.

The PP ensemble experiments were conducted with three different cumulus convection schemes: the Yoshimura, the prognostic Arakawa–Schubert, and the Kain–Fritsch schemes [see details in Murakami et al. (2012)]. The target of the PP ensemble experiments was the sensitivity of tropical cyclone projection to cumulus convection schemes. It will be discussed in section 5c.

b. Wave climate projection

Global wave climate projection was carried out by WAVEWATCH III, version 3.14 (Tolman 2009), forced by sea surface wind from MRI-AGCM3.2H. WAVEWATCH III has been used for hindcast, nowcast, and future global wave projection studies (HE13; FA13).

The global domain was set for the latitudinal range of 90°S–67°N over all longitudes with 1° × 1° spatial grids. The directional resolution is 15°, and the frequency space is 0.04–0.5 Hz, which is discretized in 25 increments logarithmically as a conventional setup. The Tolman and Chalikov (1996) source term package was used as a set for wind input and dissipation. WAVEWATCH III can represent unresolved islands (Tolman 2009). The nesting in the WNP (11°–50°N, 121°–160°E) was performed with 0.5° spatial resolution and 10° directional resolution. Sea ice was not considered in this wave climate simulation.

Ensemble experiments of wave climate projection were organized as 3 present climate experiments based

TABLE 2. Comparison of H_s between buoy observation, HPA, and ERA-Interim; the comparison is based on average, 50%, 90%, and 99% quantiles of H_s (m).

Buoy No.	Lat, lon	Source	Avg	50%	90%	99%
21004	29.0°N, 135.0°E	Buoy	1.8	1.6	3.1	5.8
		HPA	1.9	1.7	3.2	5.4
		ERA-Interim	1.8	1.6	2.8	4.7
22001	28.1°N, 126.2°E	Buoy	1.7	1.4	2.9	5.3
		HPA	1.6	1.4	2.9	4.9
		ERA-Interim	1.7	1.4	2.8	4.6
41010	28.9°N, 78.5°W	Buoy	1.6	1.4	2.6	4.4
		HPA	1.4	1.2	2.5	3.8
		ERA-Interim	1.4	1.3	2.3	3.7
44004	38.5°N, 70.4°W	Buoy	2.1	1.7	3.8	6.3
		HPA	2.0	1.7	3.6	5.9
		ERA-Interim	1.9	1.6	3.4	5.3
44011	41.1°N, 66.6°W	Buoy	2.0	1.7	3.6	6.1
		HPA	2.0	1.7	3.7	6.1
		ERA-Interim	2.0	1.7	3.5	5.5
46001	56.3°N, 148.0°W	Buoy	2.7	2.4	4.6	7.1
		HPA	2.9	2.6	5.1	7.7
		ERA-Interim	2.5	2.2	4.1	6.1
46003	51.8°N, 155.8°W	Buoy	3.0	2.7	5.1	7.7
		HPA	3.4	3.1	5.7	8.7
		ERA-Interim	3.0	2.7	4.8	7.1
46006	40.9°N, 137.5°W	Buoy	2.8	2.4	4.8	7.5
		HPA	3.0	2.6	5.2	7.7
		ERA-Interim	2.8	2.5	4.6	6.8
46035	57.1°N, 177.7°W	Buoy	2.6	2.3	4.8	7.7
		HPA	2.7	2.3	5.1	7.8
		ERA-Interim	2.5	2.2	4.3	6.6
51001	23.4°N, 162.3°W	Buoy	2.4	2.2	3.6	5.5
		HPA	2.4	2.2	3.8	5.7
		ERA-Interim	2.3	2.2	3.3	4.6
51003	19.0°N, 160.6°W	Buoy	2.2	2.1	3.1	4.3
		HPA	2.1	1.9	3.1	4.5
		ERA-Interim	2.1	2.0	2.9	3.8
51002	17.1°N, 157.8°W	Buoy	2.4	2.3	3.2	4.3
		HPA	2.2	2.1	3.0	4.0
		ERA-Interim	2.2	2.2	2.9	3.7
51004	17.5°N, 152.4°W	Buoy	2.4	2.3	3.2	4.3
		HPA	2.3	2.2	3.0	4.1
		ERA-Interim	2.3	2.2	2.9	3.7

on the 3 PP ensemble experiments and 12 future climate experiments based on 3 PP ensemble experiments and 4 SST ensemble experiments. However, in section 4, section 5a, and section 5b, the results of the SST ensemble experiments with only YS are shown in order to focus on the effect of SST differences. In section 5c, the results of PP ensemble experiments are shown in order to estimate the effect of SST differences relative to perturbed physics. The climate simulation for the present climate condition is denoted as HPA, and those for future climate conditions with SST clusters 0–3 are denoted HFAc0, HFAc1, HFAc2, and HFAc3, respectively.

3. Validation

To clearly illustrate the accuracy of the simulated wind and wave fields—namely, the sea surface wind speed at 10-m and significant wave height—the HPA was validated against reanalysis dataset and buoy observations. The European Centre for Medium-Range Weather Forecasts (ECMWF) interim reanalysis (ERA-Interim; Dee et al. 2011) was used for this validation. The performances of multimodel global wave climate simulations (Wang and Swail 2006; MO10; HE13; FA13; SE13) were compared with ERA-Interim by Hemer et al. (2013a).

Figures 2a and 2b show $\overline{U_{10}}$ for the HPA and the ERA-Interim dataset for the years 1979–2009. The spatial distribution of $\overline{U_{10}}$ of the HPA shows good qualitative agreement with that for the ERA-Interim data. The HPA can represent spatial characteristics in the historical global wind climate, such as strong winds in the Southern Ocean, relatively strong trade winds, and so on (Figs. 2a,b). Figure 2c shows the $\overline{U_{10}}$ differences between the HPA and ERA-Interim dataset. Compared with the ERA-Interim data, the $\overline{U_{10}}$ for the HPA has positive biases over almost the entire ocean (92% of the whole domain). The differences between $\overline{U_{10}}$ for the HPA and ERA-Interim are up to about $1\,\mathrm{m\,s^{-1}}$.

Figures 3a and 3b show $\overline{H_s}$ for the HPA and ERA-Interim dataset during the years 1979–2009. Similar to $\overline{U_{10}}$, $\overline{H_s}$ for the HPA can represent the historical global wave climate qualitatively. However, $\overline{H_s}$ for the HPA is larger than for ERA-Interim in almost the entire ocean (87% of the whole domain; Fig. 3c). These positive biases are remarkable in higher latitudes above 30° in both hemispheres. The positive biases are up to 0.4 m in the North Pacific, 0.7 m in the North Atlantic, and 1 m in the Southern Ocean. A result of the seasonal analysis (not shown) shows increased bias in the winter when wave heights are larger, indicating that the HPA overestimates high waves more than the ERA-Interim dataset.

In addition to the ERA-Interim, H_s and U_{10} for the HPA were compared with long-term observations by moored buoys in the Northern Hemisphere. The data were obtained from the Japanese Meteorological Agency (www.data.jma.go.jp/gmd/kaiyou/db/vessel_obs/data-report/html/buoy/buoy_NoS2_e.html) and the NOAA National Data Buoy Center (www.ndbc.noaa.gov/). The present climate results were compared with the data from 13 buoys, and two representative results of the comparisons are shown in Fig. 4. Figure 4 shows quantile–quantile plots (1%, 2%, … , 98%, 99%) of H_s and U_{10} derived from the HPA, ERA-Interim, and the relevant
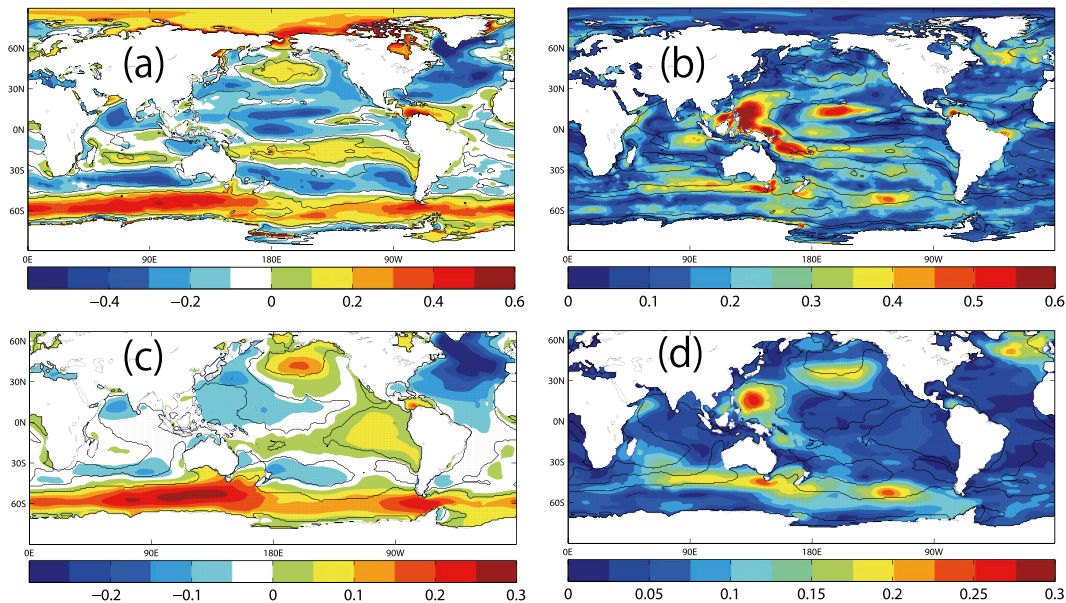
FIG. 5. Future changes in annual $\overline{U_{10}}$ and $\overline{H_s}$. (a) Ensemble mean of future changes in $\overline{U_{10}}$ (m s^{-1}); (b) maximum differences of future changes in $\overline{U_{10}}$ (m s^{-1}); (c) ensemble mean of future changes in $\overline{H_s}$ (m); and (d) maximum differences of future changes in $\overline{H_s}$ (m). Regions with black dots indicate areas where the four future projections of HFAc0–HFAc3 show the same sign.

buoys at midlatitude (56.3°N, 147.9°W; buoy 46001) and the subtropics (23.4°N, 162.3°W; buoy 51001). The observed $\overline{H_s}$ at 46001 is 2.7 m, but the HPA and ERA-Interim give 2.9 and 2.5 m, respectively. Overall, the simulated H_s from the HPA is larger than that from the buoy data, although the H_s from ERA-Interim is smaller than that of the buoy. The overestimation of H_s by HPA and underestimation by ERA-Interim are remarkable at higher quantile values, generally. On the other hand, $\overline{H_s}$ from the HPA shows good agreement with the buoy data at lower-latitude locations (i.e., 51001). Large waves can be simulated well by the HPA when compared with the ERA-Interim. Comparing the HPA and ERA-Interim data with other buoy observations in the Northern Hemisphere show similar results as described above, such as relatively large positive biases with higher wave heights in midlatitudes and better agreement with average and high wave heights at lower latitudes. The comparison of H_s between buoy, HPA, and ERA-Interim is summarized in Table 2.

The overestimation of H_s by HPA in higher latitudes can be mainly attributed to the overestimation of U_{10} by HPA (Figs. 2c, 4c), and another source of error is the wave model itself. In this study, the Tolman and Chalikov (1996) source term package in WAVEWATCH III was used as wind input and dissipation source term. There are newly proposed source term packages (e.g., Bidlot 2012; Ardhuin et al. 2010). The wave climate simulations

with the other source term packages give results different from those of Tolman and Chalikov (1996). Moreover, the wave–wave interactions and spatial and directional spectrum resolutions can influence the accuracy of wave climate simulation. However, further investigation of wave modeling is beyond this study.

An additional reason why HPA overestimates wave height when compared to ERA-Interim at high latitudes, especially over the Southern Ocean, is due to sea ice effects. Because of the lack of sea ice information for the HPA wave simulation, a broader open ocean without sea ice has longer fetch, leading to larger waves. These waves can propagate to the tropics. Ardhuin et al. (2011) indicated that wave blocking even by icebergs significantly reduces wave model errors in the region south of 45°S. Furthermore, future changes in sea ice have significant impacts on those in wave climate. SE13 showed that the future sea ice retraction would lead to an increase in wave height over the ice-retreating area in the future climate. On the other hand, an increase in sea ice (Eisenman et al. 2014) can lead to a decrease in wave height. Stocker et al. (2013) stated that a decrease in sea ice extent and volume is expected in the Antarctic but with low confidence. Therefore, discussion of wave climate projection around the sea ice region and even the tropics, where swells from the sea ice region in the Southern Ocean might be significant, requires caution. Thus, the global wave climate is simply discussed in
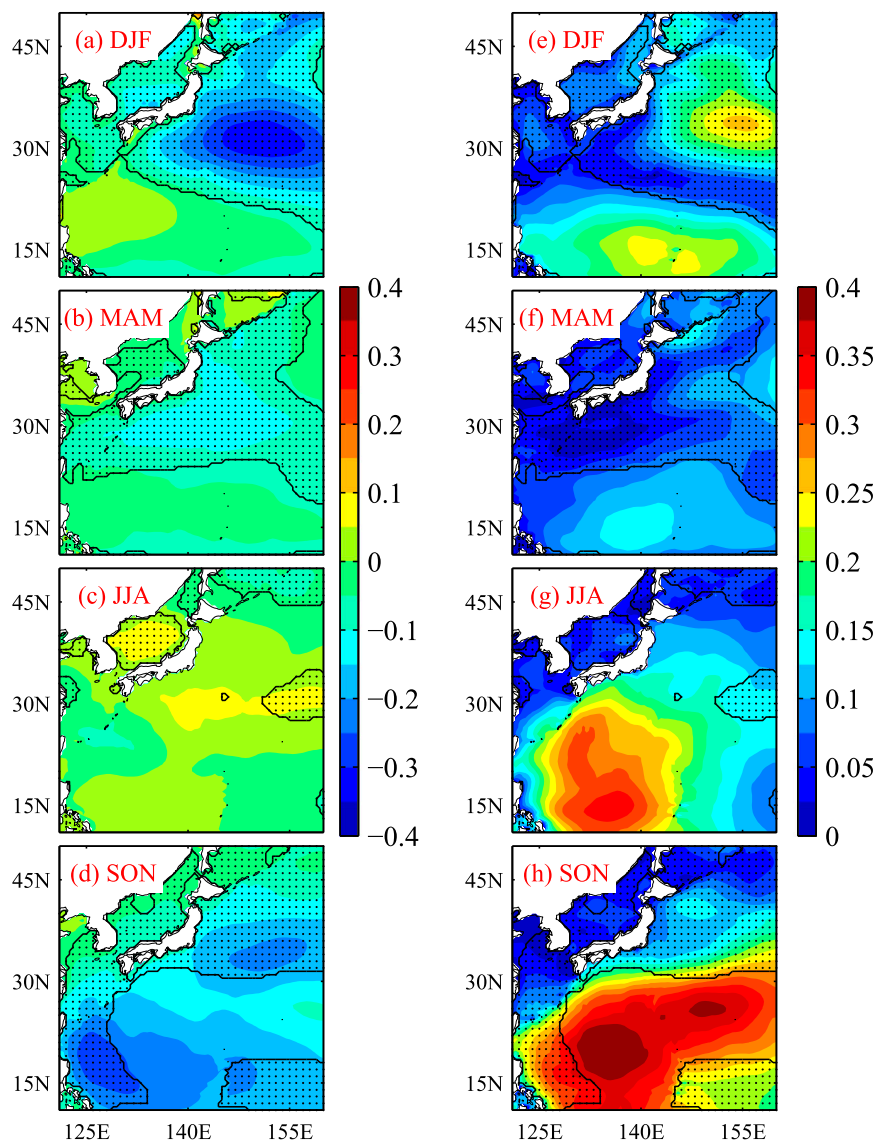
FIG. 6. Future changes in $\overline{H_s}$ for the WNP during (a) DJF, (b) MAM, (c) JJA, and (d) SON; and the maximum differences in future changes during (e) DJF, (f) MAM, (g) JJA, and (h) SON (m). Regions with black dots indicate areas where the four future projections show the same sign.

section 4, and the WNP wave climate that is unlikely to be affected by the lack of sea ice is discussed in detail in section 5.

4. Future changes in global wind and wave climate

This section simply looks at future changes in $\overline{U_{10}}$ and $\overline{H_s}$ on the global scale and the sensitivity to SST conditions. Figure 5 shows the ensemble mean and maximum differences of future changes in $\overline{U_{10}}$ and $\overline{H_s}$. Ensemble mean and maximum differences are represented as

$(\sum_{i=0}^{3} \text{HFAc}i - \text{HPA})/4$ and $\max_{i=0,1,2,3}(\text{HFAc}i - \text{HPA}) - \min_{i=0,1,2,3}(\text{HFAc}i - \text{HPA})$, respectively. In the figure, the black contoured regions with dots indicate the regions where future changes of HFAc0 through HFAc3 show the same signs (positive or negative) for reliability of projections. In regions where future changes of HFAc0 through HFAc3 show both different signs and larger differences, these areas have large uncertainty in the projected wave height, which is related to the uncertainty in SST condition.
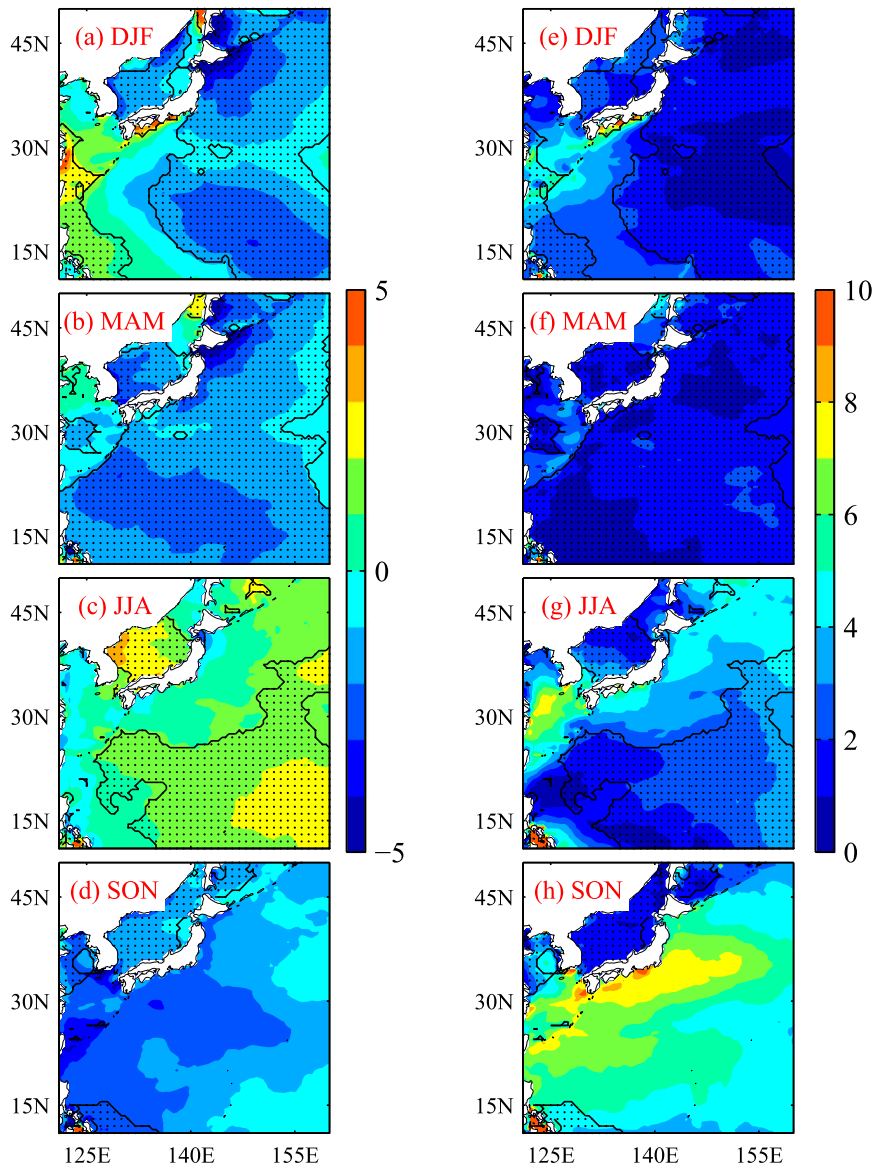
FIG. 7. Future changes in $\overline{T_p}$ (normalized by HPA value) for the WNP during (a) DJF, (b) MAM, (c) JJA, and (d) SON; and the maximum differences in future changes during (e) DJF, (f) MAM, (g) JJA, and (h) SON (%). Regions with black dots indicate areas where the four future projections show the same sign.

The spatial distributions of future changes in $\overline{U_{10}}$ and $\overline{H_s}$ are similar, which can be characterized by the changes depending on latitudes, such as increases over tropics and higher latitudes and decreases over sub-tropics (Figs. 5a,c). However, that of $\overline{U_{10}}$ depends on latitude more clearly than that of $\overline{H_s}$. This is because of increased swell height from higher latitudes, which can cancel out the decrease in wind–wave height over the subtropics. Furthermore, decreases in $\overline{U_{10}}$ and $\overline{H_s}$ are remarkable in the North Atlantic. The spatial distribution of future changes in $\overline{H_s}$ is consistent with previous

studies (Hemer et al. 2013a), except for increases over the North Pacific. Although caution is necessary for the magnitudes because of the lack of sea ice described in section 3, future changes in $\overline{U_{10}}$ and $\overline{H_s}$ are about $\pm 0.6 \, \mathrm{m \, s^{-1}}$ and $\pm 0.3 \, \mathrm{m}$, respectively, depending on the region, and the maximum differences are up to about $0.6 \, \mathrm{m \, s^{-1}}$ and $0.3 \, \mathrm{m}$ for $\overline{U_{10}}$ and $\overline{H_s}$, respectively. Therefore, the uncertainty of the $\overline{U_{10}}$ and $\overline{H_s}$ projection has the same magnitude as its future change.

The spatial distribution of maximum differences in $\overline{H_s}$ future change does not correspond to that of $\overline{U_{10}}$ in
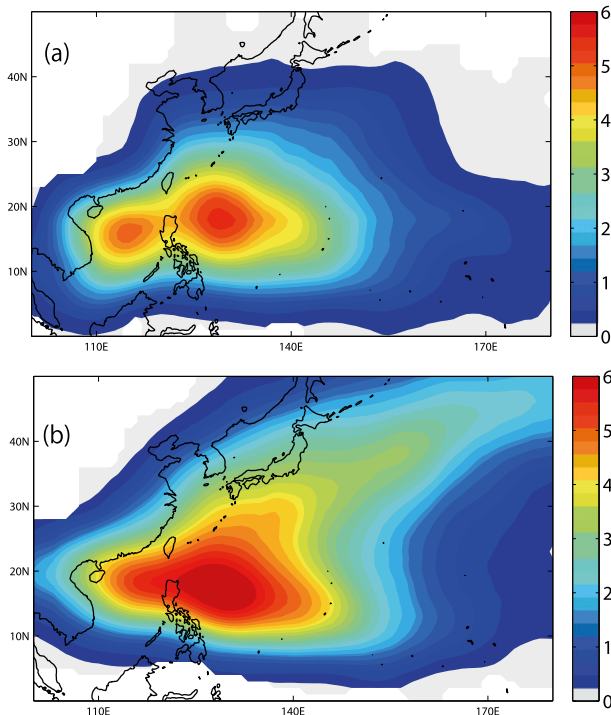
FIG. 8. Averaged frequency of typhoon passing over a smoothed $6° \times 6°$ grid in JJASON: (a) HPA and (b) best track (No. per one season).

lower latitudes (Figs. 5b,d). Wave height is roughly proportional to wind speed squared, and wind speed is relatively low in lower latitudes. Therefore, relatively larger maximum differences of future changes in $\overline{U_{10}}$ over lower latitudes (Fig. 5b) cannot contribute to those of $\overline{H_s}$ (Fig. 5d). The regions where the four future changes in $\overline{U_{10}}$ and $\overline{H_s}$ of HFAc0 through HFAc3 show the same sign account for 49.5% and 42.5% of the whole domain. The regions where the future changes of HFAc0 through HFAc3 show different signs and larger differences for both $\overline{U_{10}}$ and $\overline{H_s}$ are the lower latitudes of the WNP and the midlatitudes of the South Pacific (Figs. 5b,d). The large uncertain region in the lower latitudes of the WNP is discussed in the next section.

5. Future changes in wave climate over the western North Pacific and its relationship with typhoon characteristics and SST conditions

a. Future changes in wave climate by SST ensemble

Wave climate changes over the WNP are discussed in detail in this section. Wave climate projection data calculated by a nested 0.5° spatial resolution (section 2b) are used. Figure 6 shows the future changes in seasonal $\overline{H_s}$ and the maximum differences in the ensembles over

the WNP. The four seasons are classified as December–February, March–May, June–August, and September–November. The biggest changes in the future wave climate can be seen around 30°N, 150°E during DJF, where the $\overline{H_s}$ decrease is 0.3 m (Fig. 6a). However, there are no significant changes of H_s during MAM and JJA (Figs. 6b,c). The future changes for HFAc0–HFAc3 around the Japanese coast show the same sign during all seasons except for JJA. During MAM, the values of the maximum differences in future change are the smallest. The uncertainty in the lower latitudes of 30°N during JJA and SON is larger. For example, the future changes in $\overline{H_s}$ at 20°–30°N, 130°–150°E during SON are -0.24, -0.24, -0.23, and $+0.07$ m for HFAc0–HFAc3, respectively. The results for HFAc0–HFAc2 are consistent with each other; only the future changes of HFAc3 are different. In addition to wave height (Fig. 6), Fig. 7 shows the future changes in seasonal mean wave period [peak period (T_p)] and the maximum differences in the ensembles. Note that the future changes shown in Fig. 7 are normalized by HPA values. As with wave height, the maximum differences of seasonal mean T_p ($\overline{T_p}$) future changes are larger in JJA and SON, especially in SON. The $\overline{T_p}$ future changes by HFAc0–HFAc2 are negative over the WNP, and those by HFAc3 are positive. The seasons JJA and SON in the WNP are active typhoon seasons. Therefore, future changes in wave climate and the large uncertainty in these seasons (JJA and SON) are discussed in relation to typhoon characteristics below.

b. The relationship between future changes in wave height and typhoon characteristics

The most active area of formation of tropical cyclones over the globe is the WNP. We focus on the analysis for JJA and SON jointly [June–November (JJASON)] in the WNP to discuss typhoon effects. The typhoon detection method adopted in the present study employed the five criteria of relative vorticity at 850 hPa, temperature anomaly in the warm core region, maximum wind velocity at 850 hPa, maximum wind velocity at 300 hPa, and cyclone duration, to identify typhoons (Murakami et al. 2012). The total number of typhoon genesis cases was controlled by changing the thresholds of the criteria. The typhoon data detected by Murakami et al. (2012) were used in this study. In this subsection, data from 1979 to 2003 (and not 1979–2009) were used as the HPA. Figure 8 shows the averaged frequencies of typhoons passing from the HPA and the best-track data during 1979–2003 provided by the Japan Meteorological Agency (www.jma.go.jp/jma/jma-eng/jma-center/rsmc-hp-pub-eg/besttrack.html). The frequency was smoothed over a
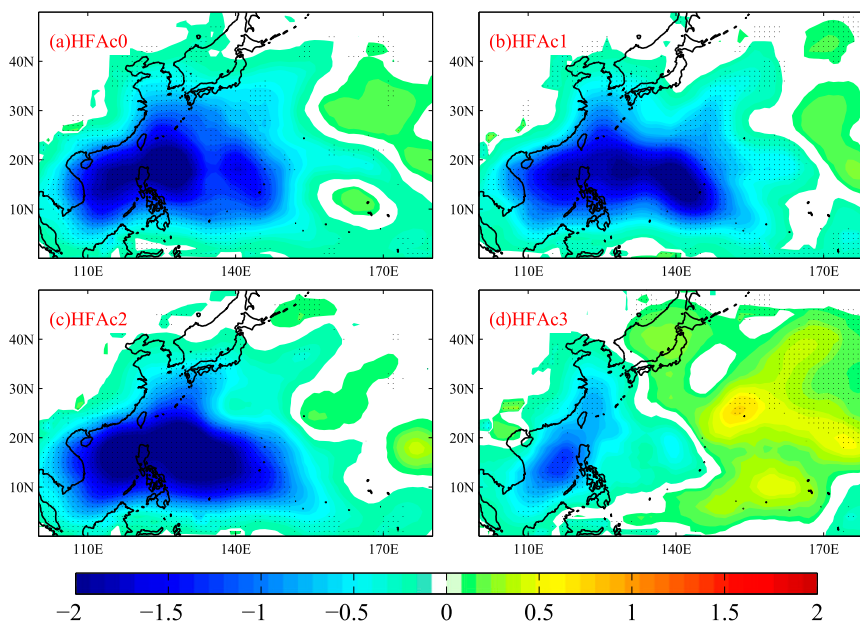
FIG. 9. Future changes in the frequency of typhoon passing in JJASON for (a) HFAc0, (b) HFAc1, (c) HFAc2, and (d) HFAc3 (No. per one season). Regions with black dots indicate significant changes with the 5% significance level tested by a Mann–Whitney U test.

$6° \times 6°$ grid. The typhoons frequently pass through the region 10°–30°N, 110°–140°E when compared with other regions. The results of the HPA show good agreement with the best track in this region. However, the HPA underestimates typhoon frequency in higher latitudes of 30°N.

Figure 9 displays the future changes in typhoon frequency for HFAc0–HFAc3. The results for HFAc0, HFAc1, and HFAc2 show less typhoon frequency in the active typhoon region. On the other hand, the reduction in typhoon frequency for HFAc3 is moderate compared with the other three experiments. As indicated in section 5a, the tendency of future $\overline{H_s}$ changes for HFAc3 is different from that of the other experiments. It can be considered that these differences of $\overline{H_s}$ changes between HFAc3 and the other experiments are caused by the differences in future changes of typhoon frequency between the ensembles, as shown by Fig. 9. However, the contributions of typhoon changes to $\overline{H_s}$ changes are not quantitatively clear. Therefore, how changes in typhoon characteristics affect the $\overline{H_s}$ was estimated quantitatively as follows. The total $\overline{H_s}$ is represented as a combination of both typhoon and nontyphoon events:

$$\overline{H_s} = \overline{H_{tc}} r_{tc} + \overline{H_{no}} (1 - r_{tc}), \qquad (1)$$

where $\overline{H_{tc}}$ is the $\overline{H_s}$ under a typhoon condition (i.e., typhoon wave intensity), $\overline{H_{no}}$ is the $\overline{H_s}$ under a nontyphoon condition (i.e., nontyphoon wave intensity), and r_{tc} is the

ratio for the period of the timeframe under a typhoon condition to the entire timeframe (i.e., typhoon frequency). Equation (1) can be rewritten for the future change in $\overline{H_s}$ as

$$\begin{aligned} \Delta\overline{H_s} &= (\overline{H_{tc}} - \overline{H_{no}})\Delta r_{tc} + \Delta\overline{H_{tc}} r_{tc} + \Delta\overline{H_{no}}(1 - r_{tc}) \\ &\quad + (\Delta\overline{H_{tc}} - \Delta\overline{H_{no}})\Delta r_{tc} \\ &= C_r + C_{Htc} + C_{Hno} + C_\Delta, \end{aligned} \qquad (2)$$

where Δ means future change; and C_r, C_{Htc}, C_{Hno}, and C_Δ are contributions of Δr_{tc} (i.e., typhoon frequency change), $\Delta\overline{H_{tc}}$ (typhoon wave intensity change), $\Delta\overline{H_{no}}$ (nontyphoon wave intensity change), and the residual to $\Delta\overline{H_s}$. Figure 10 shows $\Delta\overline{H_s}$, C_r, C_{Htc}, and C_{Hno} for HFAc0–HFAc3. The figure clearly shows that the $\Delta\overline{H_s}$ for HFAc3 are different from the other experiments (Figs. 10a–d), as described above. The $\Delta\overline{H_s}$ for HFAc0–HFAc2 show decreases in wave height by 0.3 m, but for HFAc3 they show an increase by 0.1 m. The values of C_r at lower latitudes are negative for all experiments because of a reduction in typhoon frequency in the future projection, but C_r for HFAc3 are relatively moderate compared to the others (Figs. 10e–h), which follows the result of Fig. 9. Furthermore, C_{Htc} for HFAc3 are larger than for the other experiments (Figs. 10i–l). As a result, the differences in typhoon frequency (C_r) and typhoon wave intensity changes (C_{Htc}) between HFAc3 and HFAc0–HFAc2 yield the differences in $\overline{H_s}$ future changes. Note that in the mid to higher latitudes
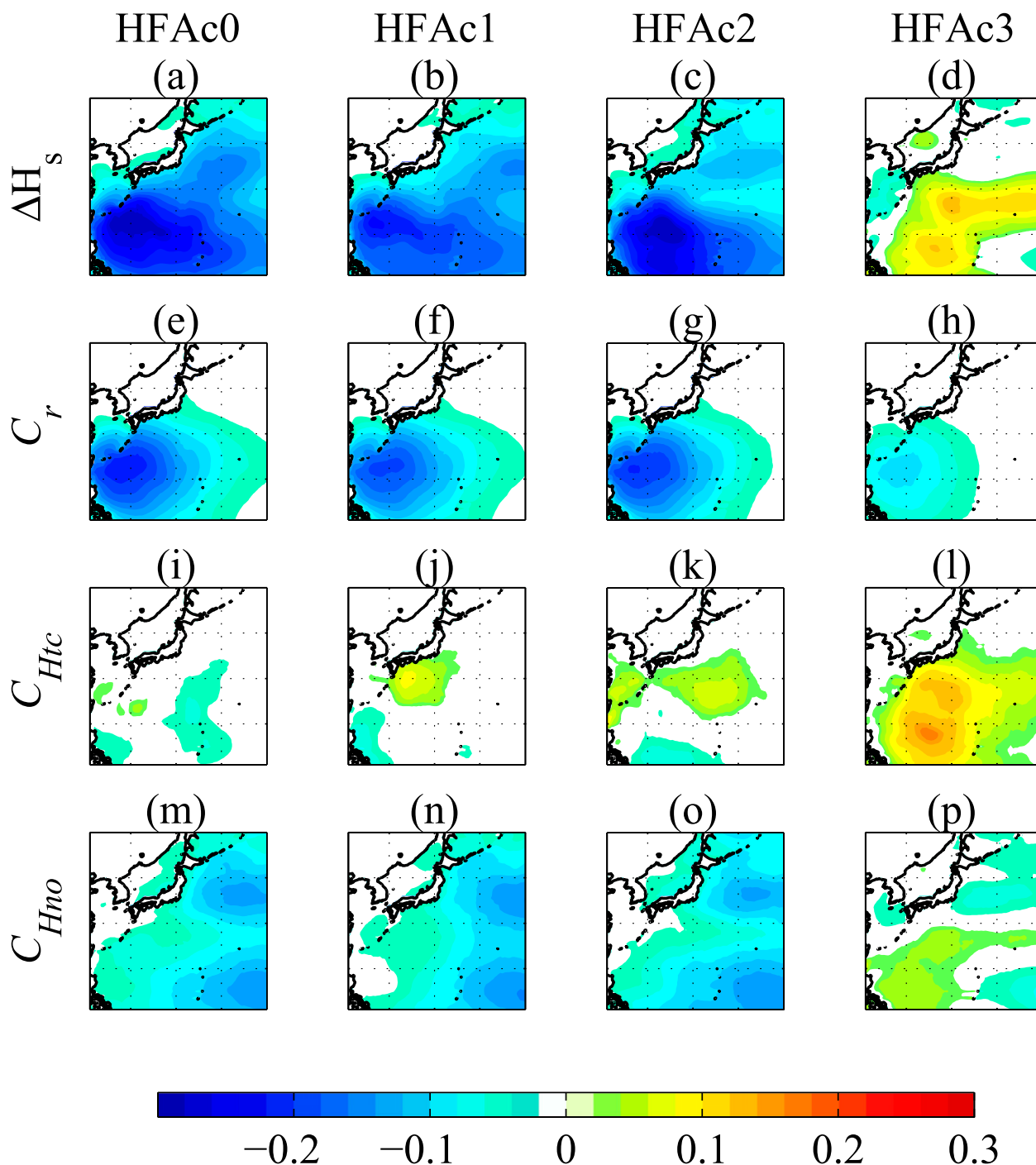
FIG. 10. Future changes in $\overline{H_s}$ for the WNP and the contributions of typhoon characteristics changes (m). (a)–(d) Future changes in $\overline{H_s}$, (e)–(h) contributions of typhoon frequency change, (i)–(l) contributions of typhoon wave intensity change, and (m)–(p) contributions of nontyphoon wave intensity change for (left)–(right) results by SST ensemble for clusters 0–3.

in Fig. 10, the influence of changes in typhoon characteristics on $\Delta\overline{H_s}$ is less accurate, because the HPA underestimates typhoon frequency in this region. Despite this, the general relationship behind the changes is clear.

c. Comparison with multimodel ensembles

The projections for $\overline{H_s}$ by SST ensemble clearly illustrate the influence of tropical cyclones. The SST
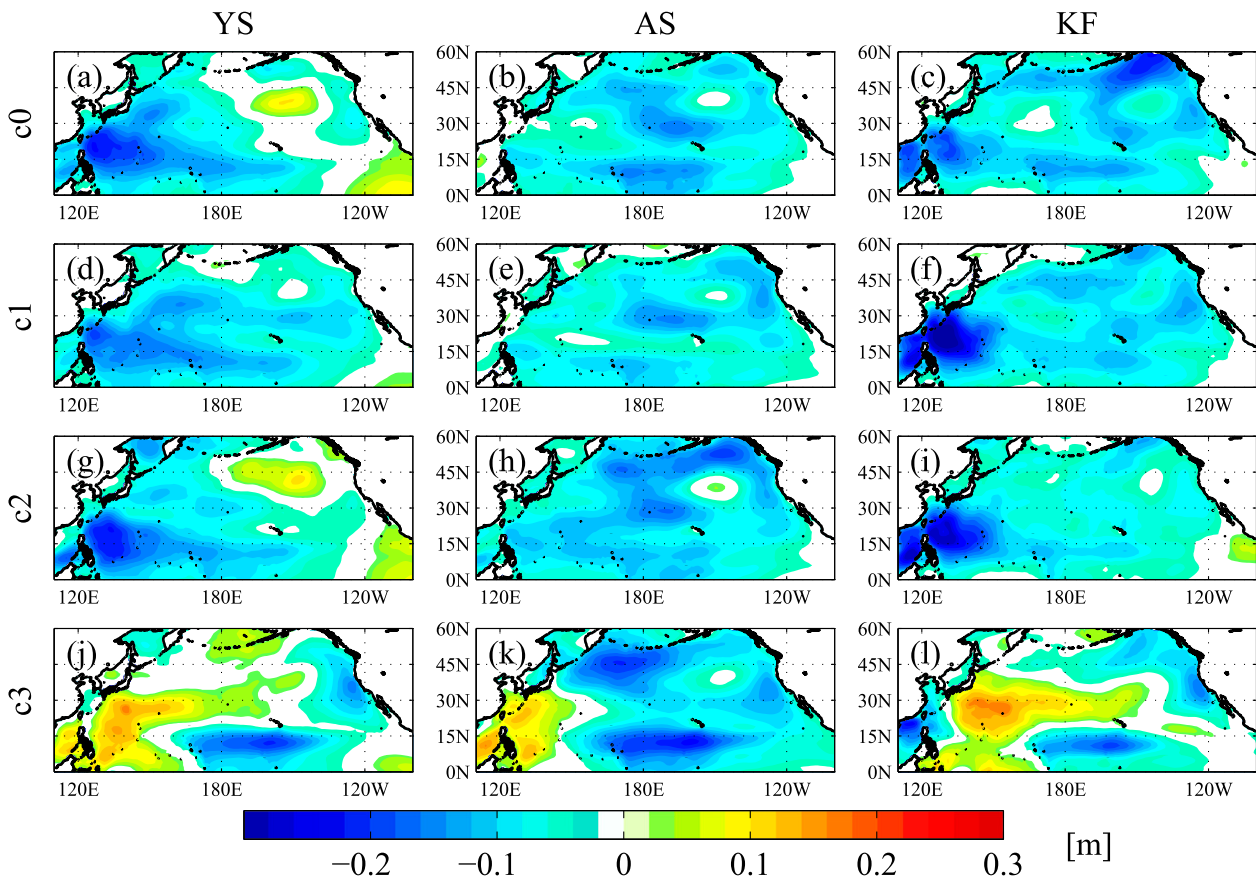
FIG. 11. Future changes in $\overline{H_s}$ during JJASON (m). (top)–(bottom) Results based on SST ensemble for clusters 0–3 from (left)–(right) perturbed physics ensemble results for YS, AS, and KF, respectively.

ensemble can perform the sensitivity analysis for a projection of SST, but the variation for future change is limited; while the multimodel ensemble gives wider variation, it is difficult to understand the reason behind the difference. Therefore, it is important to compare different types of ensembles to understand the origin of this difference and the uncertainty with forcing the projection. The multimodel ensemble experiment (COWCLIP; Hemer et al. 2012, 2013a) will help to add a general understanding about contributing factors to the projections discussed above. In addition to SST ensemble projections, PP ensemble projections were conducted with three different cumulus convection schemes (YS, AS, and KF). Note that the results shown in the above section are based on YS, as described in section 2.

Figure 11 shows the future changes in $\overline{H_s}$ using SST and PP ensemble projections during JJASON. The $\overline{H_s}$ changes for HFAc0–HFAc2 (Fig. 11, except for Figs. 11j–l) are negative in lower latitudes of the WNP, while those for HFAc3 (Figs. 11j–l) are positive. This result confirms that, in lower latitudes of the WNP, future $\overline{H_s}$ changes during summer for HFAc3 are opposite

in sign to those for HFAc0–HFAc2, and this does not depend on the cumulus convection scheme. Figure 12a shows the maximum differences in $\overline{H_s}$ changes over the 12 ensemble members, indicating that the variation of $\overline{H_s}$ changes over lower latitudes of the WNP is greatest in the North Pacific.

This result is compared with the multimodel ensemble wave climate projection data (COWCLIP, which consists of works by MO10, HE13, FA13, and SE13); the data were obtained at the COWCLIP Wiki website (https://wiki.csiro.au/display/sealevel/COWCLIP+Contributions). Although COWCLIP includes both dynamical and statistical wave climate projection data, the dynamical wave climate projection data were used in this comparison. The first reason is that the seasonal $\overline{H_s}$ was calculated by the statistical wave model with seasonal mean SLP (Wang and Swail 2006). Therefore the statistical wave model could not resolve typhoon-generated waves. Second, the statistical wave climate projection was forced by the sea level pressure (SLP) of AOGCM. Therefore, SST was not used as a boundary condition in comparison with the dynamical projections.
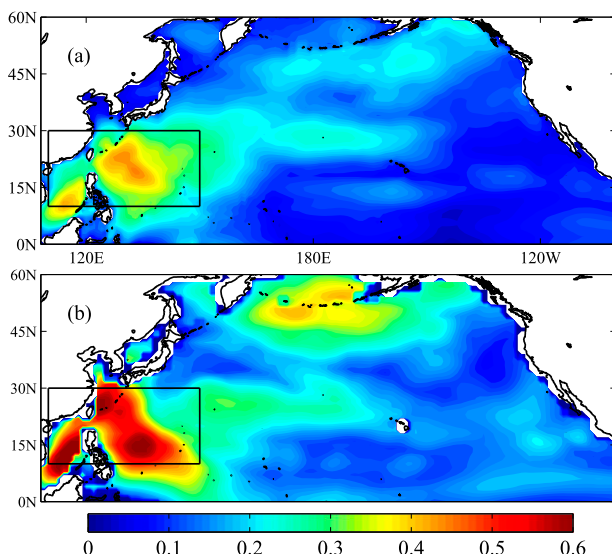
FIG. 12. Maximum differences in future changes of $\overline{H_s}$ during JJASON over ensemble members (m). (a) The 12 members of SST and PP ensemble projections and (b) the 6 members from COWCLIP analyses.

HE13 and FA13 provided two members from each study, because of two different SST conditions, which are denoted as HE13(1), HE13(2), FA13(1), and FA13(2), respectively. When those members are counted with members from MO10 and SE13, they total six COWCLIP projections. The COWCLIP projections were conducted based on the dynamical approach, which is described in the introduction, and the same framework as this study; however, the components of the framework are different from each other. The main components are the future emission scenario, the SST condition for the AGCM, the AGCM, and the wave model. The description of the wave climate projections for COWCLIP is shown in Table 3, focusing on the components and the SST cluster number. The six wave projections for COWCLIP are quite different from each other in that they use different SST conditions for the AGCM, SRES scenarios, AGCMs, and wave models (Table 3). Although they are different, the maximum differences in future changes of $\overline{H_s}$ across the COWCLIP projections shown in Fig. 12b give a similar

spatial distribution to that for this study in Fig. 12a. Although the magnitude is different, the spatial distributions are characterized by a greater maximum difference in the lower latitudes of the WNP. This indicates that the COWCLIP projections also have a large uncertainty with the changes in the future wave climate, likely related with typhoon changes.

Future changes in $\overline{H_s}$ for the SST, PP ensemble, and COWCLIP projections for the region demarcated in Fig. 12 (10°–30°N, 110°–150°E) are shown in Fig. 13. It is clear that future changes under SST cluster 3 of this present study have a different tendency when compared to those under clusters 0, 1, and 2; and future changes under FA13(1) are also different from the other COWCLIP projections. The wave climate projection from FA13(1) is based on SST projected by GFDL CM2.1 under the A1B scenario, which is classified into SST cluster 3 by clustering analysis (Tables 1 and 3). FA13(2) and the MO10 member are based on the CMIP3 ensemble SST under A1B, which can be classified into cluster 0; the SE13 member is based on the SST from MPI's ECHAM5 under A1B, which can be classified into cluster 2 (Tables 1 and 3). HE13(1) and HE13(2) are based on the SST of ECHAM5 and CSIRO Mk3.5 under the A2 scenario (Table 3) and have not been clustered by Murakami et al. (2012) because the analysis of Murakami et al. (2012) was for the A1B scenario; but the SST patterns of HE13(1) and HE13(2) correlate relatively well with clusters 2 and 1, respectively, when compared with the other SST clusters.

Therefore, the SST ensemble results show that in the lower latitudes of the WNP future $\overline{H_s}$, changes forced by the SST cluster 3 condition are positive, and those forced under the other SST cluster conditions are negative, results that are consistent with COWCLIP projections. In addition to FA13(1) and FA13(2), FA13 has conducted additional wave climate projections forced by SSTs projected by ECHAM5 and HadCM3 under an A1B scenario (which are clusters 2 and 3, Table 1), indicating that in the western Pacific during the summer months, future changes in $\overline{H_s}$ under the SST cluster 3 condition (HadCM3 and GFDL CM2.1) are larger than those for clusters 0 and 2 (CMIP3 ensemble mean and

TABLE 3. Model description of the present study and COWCLIP (Hemer et al. 2013a).

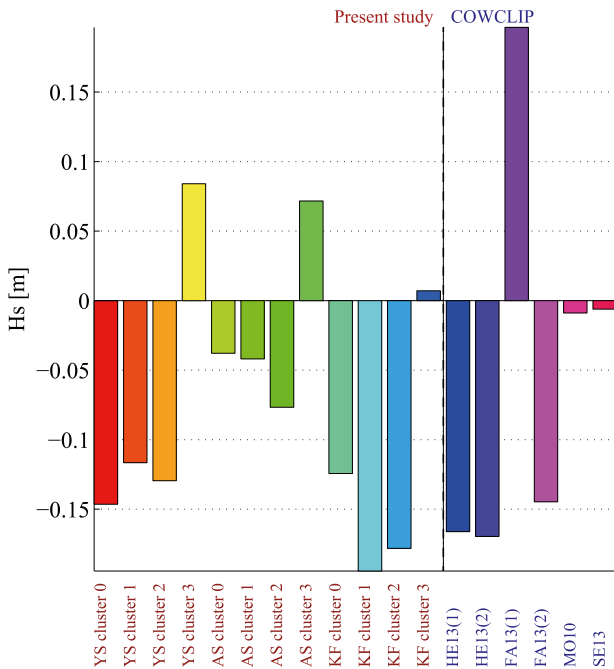|	This study	HE13(1)	HE13(2)	FA13(1)	FA13(2)	MO10	SE10
Reference	—	HE13		FA13		MO10	SE13
Scenario	A1B	A2		A1B		A1B	A1B
SST	4 clusters	ECHAM5	CSIRO Mk3.5	GFDL CM2.1	CMIP3 mean	CMIP3 mean	ECHAM5
AGCM	MRI-AGCM3.2H	CSIRO's CCAM		GFDL's HiRAM and WW3 coupled		MRI-AGCM3.1S	ECHAM5 AGCM
Wave model	WW3	WW3				SWAN	WAM
SST cluster No.	0–3	2	1	3	0	0	2

FIG. 13. Future changes in $\overline{H_s}$ for the present study and COWCLIP analysis for the region outlined in Fig. 12 (10°–30°N, 110°–150°E). The first 12 bars from the left are for the present study, and the remaining bars are for COWCLIP models.

FIG. 14. The relationship between the future changes in SST for the western equatorial Pacific (dSST1; 5°S–5°N, 140°E–180°) and the subtropical South Pacific (dSST2; 15°–30°S, 90°W–180°). The future changes in SST are normalized by the mean future change for the whole tropic region. Letters A through R denote the individual model runs of CMIP3 described in Table 1. Green indicates that the model SST is cluster 1, blue is cluster 2, and red is cluster 3. Letters S and T denote MPI's ECHAM5 and CSIRO Mk3.5, respectively, under the A2 scenario used by HE13.

ECHAM5), a result due to variation in the future change of typhoon frequency. This result of FA13 is also consistent with this study. In spite of the differences in the GCMs themselves and the other forcing factors, the present study's ensemble experiments yield variations in future $\overline{H_s}$ changes that are consistent with the COWCLIP ensemble. These similar deviations suggest that the major factor behind mean wave climate changes in the WNP is SST changes and the associated typhoon activity in the future climate.

As discussed above, SST as a boundary condition for AGCM has significant impact on wave climate projection. Although clustering by SST has been defined with future change patterns for the entire tropical domain, SST clusters can be characterized by the magnitudes of warming in the equatorial and subtropical Pacific, as seen in Fig. 1. Therefore, SST clusters are described simply by the relationship between the future changes in SST for two identified regions, as follows. One of the regions is the western equatorial Pacific (dSST1; 5°S–5°N, 140°E–180°), the other is the subtropical South Pacific (dSST2; 15°–30°S, 90°W–180°). Normalized future changes in SST within the two regions for CMIP3 models and clusters 1–3 are shown in Fig. 14. Normalized future change means that the future change in SST is divided by the mean future change of the whole tropical region (30°S–30°N). It is clear that SST cluster 3 can be characterized as more relative
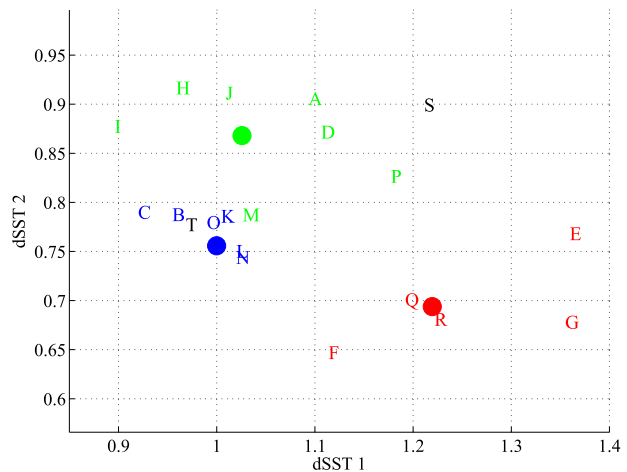
warming over the western equatorial Pacific and less relative warming over the subtropical South Pacific than other SST clusters. The physical mechanism behind the relationship between these SST characteristics and wave climates has not been addressed in this study in detail. A possible mechanism can be found in the study on the relationship between interhemispheric SST gradients and typhoons. Zhan et al. (2013) indicated that warmer SST in the western Pacific warm pool (WWP; 0°–16°N, 125°–165°E) and cooler SST in the southwestern Pacific Ocean (SWP; 20°–40°S, 160°E–170°W) during MAM induces favorable conditions for typhoon genesis and intensity. Future changes in SST differences between WWP and SWP (SST in WWP − SST in SWP) under clusters 0–3 are +0.07°, −0.05°, +0.03°, and +0.48°C. Therefore, the condition under SST cluster 3 is favorable for typhoons following the result by Zhan et al. (2013), yielding high waves when compared with the other SST clusters.

6. Conclusions

Future projections of global and WNP wave climate were conducted using an atmospheric global climate model (MRI-AGCM3.2H) and a wave model (WAVEWATCH III). To analyze the sensitivity of the projected wave climate to SST conditions, SST ensemble experiments were conducted. We used four different future SST conditions (SST cluster 0–3) as boundary conditions for MRI-AGCM3.2H. The four SST conditions were
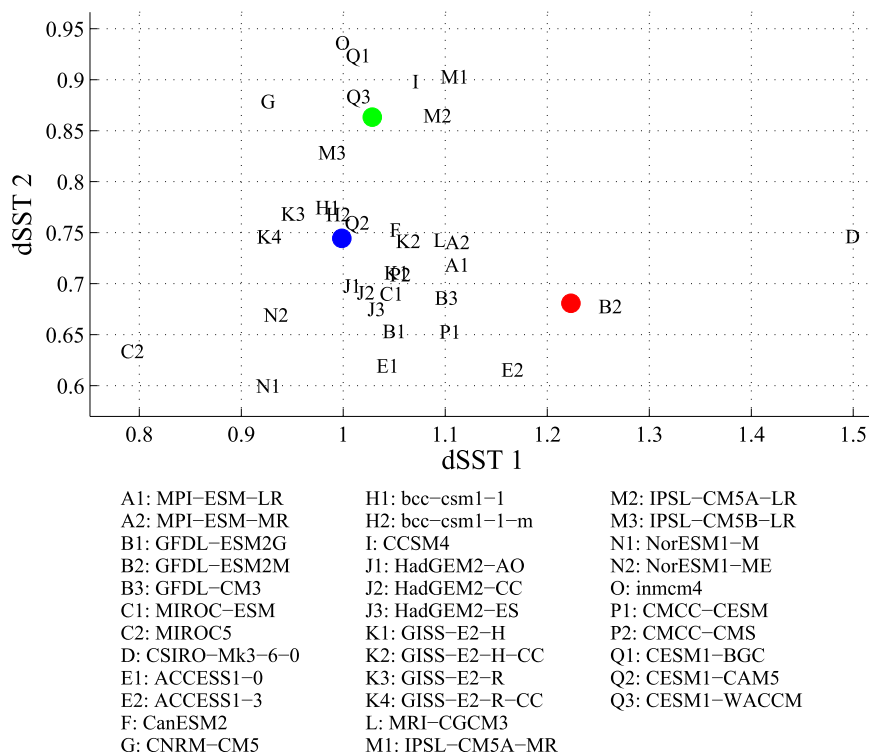
FIG. 15. As in Fig. 14, but plotted for the 34 models of CMIP5.

defined based on SST projected by 18 models from phase 3 of the Coupled Model Intercomparison Project. One of the SST conditions is the ensemble-mean SST of 18 CMIP3 models, and the other three are representative SST conditions derived from 18 CMIP3 models by applying cluster analysis to the future change patterns of SST.

Future changes in global annual $\overline{H_s}$ are about ± 0.3 m depending on the region. The regions where four future changes under four different SST conditions show the same sign cover 43% of the global domain (Fig. 5a). Although some future changes are consistent with those from previous studies, such as increases in wave height over the Southern Ocean and reductions over the North Atlantic, some particular regions show either positive or negative future change depending on SST conditions, a result indicating that the uncertainty in future projections is large. The future changes in wave height in the WNP during the summer, where variation in future changes is large, were analyzed in detail. Future changes in $\overline{H_s}$ for the lower latitudes of the WNP during the summer under SST cluster 3 are opposite in sign to those under cluster 0 to cluster 2 conditions. Future changes under the SST cluster 3 condition are positive. The SST cluster 3 condition is characterized with higher warming in the equatorial Pacific (Fig. 1).

The direct cause of these changes in future wave height is future changes in the frequency and intensity of typhoons.

This means that the variation in future changes of SST influences future changes in typhoon characteristics, and then that leads to differences in wave height in the WNP. Furthermore, it is clear that variation of SST is also a major source of uncertainty for the summertime wave climate in the WNP based on the results by perturbed physics ensemble experiments in this study and multimodel ensemble projections from previous studies (COWCLIP). The PP ensemble experiments and the COWCLIP results confirmed the relationship between the pattern for future change in SST and the wave climate in the WNP during the summer, such as the increases in the mean wave height under relatively warmer SST in the equatorial Pacific: namely, the cluster 3 condition. Delcambre et al. (2013) indicated that uncertainties in SST changes are a major source of uncertainties in the Northern Hemisphere jet stream changes, suggesting that a reduction of uncertainty in the tropical Pacific SST response to global warming will significantly reduce uncertainty in the Northern Hemisphere zonal wind response to climate change. The same holds true for wave climate, especially in the WNP during the summer.

The projected SST conditions used in this study are based on the CMIP3 dataset. The latest dataset, CMIP5 (Taylor et al. 2012), has been available for projection and impact assessments. Figure 15 shows the SST changes as in Fig. 14, but Fig. 15 uses the CMIP5 SSTs under the

representative concentration pathway 8.5 (RCP8.5) scenario. Future SST changes using CMIP5 have a similar variation to those using CMIP3 data (cf. Figs. 15 and 14). Therefore, wave climate projections based on CMIP5 can still have the uncertainty related with SST uncertainty, including the uncertainty of future changes in mean wave height over the WNP, which significantly depends on future changes in SST, as shown through this paper.

Although the details of the physical mechanism behind the relationship have not been addressed in this study, insight into what causes variations in wave projections can provide better understanding of ocean climate change. In this study, the insight into a major cause of variations in wave projections over the WNP has been presented. We will conduct further analysis of this type of problem focusing on other geographical regions, other wave properties, and an extreme wave climate.

APPENDIX

List of Abbreviations

A1B	A scenario from the IPCC SRES (Solomon et al. 2007)
A2	A scenario from the IPCC SRES (Solomon et al. 2007)
AGCM	Atmospheric global climate model
AOGCM	Atmosphere–ocean global climate model
AS	Arakawa–Schubert cumulus convection scheme
CCAM	CSIRO Cubic-Conformal Atmospheric Model
CMIP3	Phase 3 of the Coupled Model Intercomparison Project (Meehl et al. 2007)
CMIP5	Phase 5 of the Coupled Model Intercomparison Project (Taylor et al. 2012)
COWCLIP	Coordinated Ocean Wave Climate Project (Hemer et al. 2012, 2013a)
CSIRO	Commonwealth Scientific and Industrial Research Organisation
CSIRO Mk3.5	CSIRO Mark 3.5 model
DJF	December–February
ECHAM5	Global climate model developed by the Max Planck Institute (see Table 1)
FA13(x)	Wave climate projection x by FA13 (see Table 3)
GCM	Global climate model
GFDL	Geophysical Fluid Dynamics Laboratory
GFDL CM2.1	GFDL Climate Model, version 2.1 (see Table 1)
HadCM3	Met Office Hadley Centre Coupled Model, version 3 (see Table 1)
HE13(x)	Wave climate projection x by HE13 (see Table 3)
HPA	The present climate simulation (see section 2b)
HFAci	The future climate simulation under SST cluster i condition (i = 0, 1, 2, or 3; see section 2b)
H_s	Significant wave height
$\overline{H_s}$	Mean significant wave height
IPCC	Intergovernmental Panel on Climate Change
IPCC AR4	IPCC Fourth Assessment Report (Solomon et al. 2007)
IPCC AR5	IPCC Fifth Assessment Report (Stocker et al. 2013)
JJA	June–August
KF	Kain–Fritsch cumulus convection scheme
MAM	March–May
MO10	Wave climate projection by MO10 (see Table 3)
MPI	Max Planck Institute
MRI-AGCM3.2	Meteorological Research Institute Atmospheric General Circulation Model, version 3.2
PP	Perturbed physics
SE13	Wave climate projection by SE13 (see Table 3)
SON	September–November
SRES	Special Report on Emissions Scenarios (Solomon et al. 2007)
SST	Sea surface temperature
SWAN	Simulating Waves Nearshore
U_{10}	Sea surface wind speed at 10 m
$\overline{U_{10}}$	Mean sea surface wind speed at 10 m
WAM	WAM wave model
WNP	Western North Pacific
WW3	WAVEWATCH III
YS	Yoshimura cumulus convection scheme

REFERENCES

Ardhuin, F., and Coauthors, 2010: Semiempirical dissipation source functions for ocean waves. Part I: Definition, calibration, and validation. *J. Phys. Oceanogr.,* **40,** 1917–1941, doi:10.1175/2010JPO4324.1.

——, J. Tournadre, P. Queffeulou, F. Girard-Ardhuin, and F. Collard, 2011: Observation and parameterization of small icebergs: Drifting breakwaters in the southern ocean. *Ocean Modell.,* **39,** 405–410, doi:10.1016/j.ocemod.2011.03.004.

Bidlot, J.-R., 2012: Present status of wave forecasting at ECMWF. *Proc. ECMWF Workshop on Ocean Waves,* Reading, United Kingdom, 42 pp. [Available online at http://nwmstest.ecmwf.int/newsevents/meetings/workshops/2012/Ocean_Waves/presentations/Bidlot.pdf.]

Charles, E., D. Idier, P. Delecluse, M. Déqué, and G. Le Cozannet, 2012: Climate change impact on waves in the Bay of Biscay, France. *Ocean Dyn.,* **62,** 831–848, doi:10.1007/s10236-012-0534-8.

Cruz, J., 2008: *Ocean Wave Energy: Current Status and Future Perspectives.* Springer-Verlag, 431 pp.

Dee, D. P., and Coauthors, 2011: The ERA-Interim reanalysis: Configuration and performance of the data assimilation system. *Quart. J. Roy. Meteor. Soc.,* **137,** 553–597, doi:10.1002/qj.828.

Delcambre, S. C., D. J. Lorenz, D. J. Vimont, and J. E. Martin, 2013: Diagnosing Northern Hemisphere jet portrayal in 17 CMIP3 global climate models: Twenty-first-century projections. *J. Climate,* **26,** 4930–4946, doi:10.1175/JCLI-D-12-00359.1.

Dobrynin, M., J. Murawsky, and S. Yang, 2012: Evolution of the global wind wave climate in CMIP5 experiments. *Geophys. Res. Lett.,* **39,** L18606, doi:10.1029/2012GL052843.

Eisenman, I., W. N. Meier, and J. R. Norris, 2014: A spurious jump in the satellite record: Has Antarctic sea ice expansion been overestimated? *Cryosphere,* **8,** 1289–1296, doi:10.5194/tc-8-1289-2014.

Fan, Y., I. M. Held, S.-J. Lin, and X. L. Wang, 2013: Ocean warming effect on surface gravity wave climate change for the end of the twenty-first century. *J. Climate,* **26,** 6046–6066, doi:10.1175/JCLI-D-12-00410.1.

Gulev, S., and V. Grigorieva, 2004: Last century changes in ocean wind wave height from global visual wave data. *Geophys. Res. Lett.,* **31,** L24302, doi:10.1029/2004GL021040.

Hallegatte, S., C. Green, R. J. Nicholls, and J. Corfee-Morlot, 2013: Future flood losses in major coastal cities. *Nat. Climate Change,* **3,** 802–806, doi:10.1038/nclimate1979.

Hemer, M. A., J. A. Church, and J. R. Hunter, 2010: Variability and trends in the directional wave climate of the Southern Hemisphere. *Int. J. Climatol.,* **30,** 475–491, doi:10.1002/joc.1900.

——, X. L. Wang, R. Weisse, and V. R. Swail, 2012: Advancing wind-waves climate science: The COWCLIP project. *Bull. Amer. Meteor. Soc.,* **93,** 791–796, doi:10.1175/BAMS-D-11-00184.1.

——, Y. Fan, N. Mori, A. Semedo, and X. Wang, 2013a: Projected changes in wave climate from a multi-model ensemble. *Nat. Climate Change,* **3,** 471–476, doi:10.1038/nclimate1791.

——, J. Katzfey, and C. E. Trenham, 2013b: Global dynamical projections of surface ocean wave climate for a future high greenhouse gas emission scenario. *Ocean Modell.,* **70,** 221–245, doi:10.1016/j.ocemod.2012.09.008.

Hoeke, R. K., K. L. McInnes, J. Kruger, R. McNaught, J. R. Hunter, and S. G. Smithers, 2013: Widespread inundation of Pacific islands triggered by distant-source wind-waves.

Global Planet. Change, **108,** 128–138, doi:10.1016/j.gloplacha.2013.06.006.

Knutti, R., D. Masson, and A. Gettelman, 2013: Climate model genealogy: Generation CMIP5 and how we got there. *Geophys. Res. Lett.,* **40,** 1194–1199, doi:10.1002/grl.50256.

Kuriyama, Y., M. Banno, and T. Suzuki, 2012: Linkages among interannual variations of shoreline, wave and climate at Hasaki, Japan. *Geophys. Res. Lett.,* **39,** L06604, doi:10.1029/2011GL050704.

Meehl, G. A., C. Covey, K. E. Taylor, T. Delworth, R. J. Stouffer, M. Latif, B. McAvaney, and J. F. B. Mitchell, 2007: The WCRP CMIP3 multimodel dataset: A new era in climate change research. *Bull. Amer. Meteor. Soc.,* **88,** 1383–1394, doi:10.1175/BAMS-88-9-1383.

Menéndez, M., F. Méndez, I. J. Losada, and N. E. Graham, 2008: Variability of extreme wave heights in the northeast Pacific Ocean based on buoy measurements. *Geophys. Res. Lett.,* **35,** L22607, doi:10.1029/2008GL035394.

Mizuta, R., and Coauthors, 2012: Climate simulations using MRI-AGCM3.2 with 20-km grid. *J. Meteor. Soc. Japan,* **90A,** 233–258, doi:10.2151/jmsj.2012-A12.

Mori, N., T. Yasuda, H. Mase, T. Tom, and Y. Oku, 2010: Projection of extreme wave climate change under global warming. *Hydrol. Res. Lett.,* **4,** 15–19, doi:10.3178/hrl.4.15.

——, T. Shimura, T. Yasuda, and H. Mase, 2013: Multi-model climate projections of ocean surface variables under different climate scenarios—Future change of waves, sea level and wind. *Ocean Eng.,* **71,** 122–129, doi:10.1016/j.oceaneng.2013.02.016.

Murakami, H., R. Mizuta, and E. Shindo, 2012: Future changes in tropical cyclone activity projected by multi-physics and multi-SST ensemble experiments using the 60-km-mesh MRI-AGCM. *Climate Dyn.,* **39,** 2569–2584, doi:10.1007/s00382-011-1223-x.

Rayner, N., D. Parker, E. Horton, C. Folland, L. Alexander, D. Rowell, E. Kent, and A. Kaplan, 2003: Global analyses of sea surface temperature, sea ice, and night marine air temperature since the late nineteenth century. *J. Geophys. Res.,* **108,** 4407, doi:10.1029/2002JD002670.

Sasaki, W., 2012: Changes in wave energy resources around Japan. *Geophys. Res. Lett.,* **39,** L23702, doi:10.1029/2012GL053845.

Semedo, A., K. Sušelj, A. Rutgersson, and A. Sterl, 2011: A global view on the wind sea and swell climate and variability from ERA-40. *J. Climate,* **24,** 1461–1479, doi:10.1175/2010JCLI3718.1.

——, R. Weisse, A. Behrens, A. Sterl, L. Bengtsson, and H. Günther, 2013: Projection of global wave climate change toward the end of the twenty-first century. *J. Climate,* **26,** 8269–8288, doi:10.1175/JCLI-D-12-00658.1.

Short, A. D., 1999: *Handbook of Beach and Shoreface Morphodynamics.* John Wiley and Sons, 379 pp.

Solomon, S., D. Quin, M. Manning, Z. Chen, M. Marquis, K. Averyt, M. Tignor, and H. L. Miller Jr., Eds., 2007: *Climate Change 2007: The Physical Science Basis.* Cambridge University Press, 996 pp. [Available online at http://www.ipcc.ch/pdf/assessment-report/ar4/wg1/ar4_wg1_full_report.pdf.]

Stocker, T. F., and Coauthors, 2013: *Climate Change 2013: The Physical Science Basis.* Cambridge University Press, 1535 pp. [Available online at http://www.ipcc.ch/pdf/assessment-report/ar5/wg1/WG1AR5_ALL_FINAL.pdf.]

Suh, K.-D., S.-W. Kim, N. Mori, and H. Mase, 2012: Effect of climate change on performance-based design of caisson breakwaters. *J. Waterw. Port Coastal Ocean Eng.,* **138,** 215–225, doi:10.1061/(ASCE)WW.1943-5460.0000126.

Taylor, K. E., R. J. Stouffer, and G. A. Meehl, 2012: An overview of CMIP5 and the experiment design. *Bull. Amer. Meteor. Soc.,* **93,** 485–498, doi:10.1175/BAMS-D-11-00094.1.

Tolman, H. L., 2009: User manual and system documentation of WAVEWATCH III version 3.14. NOAA/NWS/NCEP/MMAB Tech. Note 276, 220 pp. [Available online at http://polar.ncep.noaa.gov/mmab/papers/tn276/MMAB_276.pdf.]

——, and D. Chalikov, 1996: Source terms in a third-generation wind wave model. *J. Phys. Oceanogr.,* **26,** 2497–2518, doi:10.1175/1520-0485(1996)026<2497:STIATG>2.0.CO;2.

Wang, X., and V. Swail, 2001: Changes of extreme wave heights in Northern Hemisphere oceans and related atmospheric circulation regimes. *J. Climate,* **14,** 2204–2221, doi:10.1175/1520-0442(2001)014<2204:COEWHI>2.0.CO;2.

——, and ——, 2006: Climate change signal and uncertainty in projections of ocean wave heights. *Climate Dyn.,* **26,** 109–126, doi:10.1007/s00382-005-0080-x.

Young, I., S. Zieger, and A. Babanin, 2011: Global trends in wind speed and wave height. *Science,* **332,** 451–455, doi:10.1126/science.1197219.

Zhan, R., Y. Wang, and M. Wen, 2013: The SST gradient between the southwestern Pacific and the western Pacific warm pool: A new factor controlling the northwestern Pacific tropical cyclone genesis frequency. *J. Climate,* **26,** 2408–2415, doi:10.1175/JCLI-D-12-00798.1.